metals

MDPI

Article

Effect of Strain Rate on Microstructure Evolution and Mechanical Behavior of Titanium-Based Materials

Pavlo E. Markovsky [1,*], Jacek Janiszewski [2], Vadim I. Bondarchuk [1], Oleksandr O. Stasyuk [1], Dmytro G. Savvakin [1], Mykola A. Skoryk [1], Kamil Cieplak [2], Piotr Dziewit [2] and Sergey V. Prikhodko [3]

[1] G.V. Kurdyumov Institute for Metal Physics of N.A.S. of Ukraine, 36 Academician Vernadsky Boulevard, UA-03142 Kyiv, Ukraine; vbondar77@gmail.com (V.I.B.); stasiuk@imp.kiev.ua (O.O.S.); savva@imp.kiev.ua (D.G.S.); mykolaskor@gmail.com (M.A.S.)

[2] Jarosław Dąbrowski, Military University of Technology, 2 gen. Sylwester Kaliski str., 00-908 Warsaw, Poland; jacek.janiszewski@wat.edu.pl (J.J.); kamil.cieplak@wat.edu.pl (K.C.); piotr.dziewit@wat.edu.pl (P.D.)

[3] Department of Materials Science and Engineering, University of California Los Angeles, Los Angeles, CA 90095, USA; sergey@seas.ucla.edu

* Correspondence: pmark@imp.kiev.ua; Tel.: +38-044-4243374

Received: 6 October 2020; Accepted: 19 October 2020; Published: 22 October 2020

Abstract: The goal of the present work is a systematic study on an influence of a strain rate on the mechanical response and microstructure evolution of the selected titanium-based materials, i.e., commercial pure titanium, Ti-6Al-4V alloy with lamellar and globular microstructures produced via a conventional cast and wrought technology, as well as Ti-6Al-4V fabricated using blended elemental powder metallurgy (BEPM). The quasi-static and high-strain-rate compression tests using the split Hopkinson pressure bar (SHPB) technique were performed and microstructures of the specimens were characterized before and after compression testing. The strain rate effect was analyzed from the viewpoint of its influence on the stress–strain response, including the strain energy, and a microstructure of the samples after compressive loading. It was found out that the Ti-6Al-4V with a globular microstructure is characterized by high strength and high plasticity (ensuring the highest strain energy) in comparison to alloy with a lamellar microstructure, whereas Ti6-Al-4V obtained with BEPM reveals the highest plastic flow stress with good plasticity at the same time. The microstructure observations reveal that a principal difference in high-strain-rate behavior of the tested materials could be explained by the nature of the boundaries between the structural components through which plastic deformation is transmitted: α/α boundaries prevail in the globular microstructure, while α/β boundaries prevail in the lamellar microstructure. The Ti-6Al-4V alloy obtained with BEPM due to a finer microstructure has a significantly better balance of strength and plasticity as compared with conventional Ti-6Al-4V alloy with a similar type of the lamellar microstructure.

Keywords: titanium alloy; high strain rate testing; split hopkinson pressure bar technique; microstructure influence; phase transformation; deformation mechanism; strain energy

1. Introduction

Titanium alloys are an important structural material used in modern aerospace, automotive, shipbuilding, and military fields, because of the high level of specific strength, fracture toughness, fatigue strength, corrosion resistance, non-magnetization, and other specific physical, mechanical, and service properties [1–4]. Since these alloys are relatively expensive, their advantages over other structural materials become more apparent when they are processed using different methods to as higher as possible values of specific strength. A separate important direction in the application of titanium

alloys, which is increasingly being used, is the manufacture of armor elements [4–6], as well as individual elements of military equipment experiencing impact or explosive loading [4,7]. Traditionally the designers of new products are based on the mechanical properties of materials, which have been determined under certain standard, mainly quasi-static test conditions. However, in most cases of machines and devices, it does not correspond to the actual operating conditions of real parts, for example, emergency conditions of heavy-loaded structural elements of airplanes subjected to strong turbulence, or the landing gear during extremely hard landings. Therefore, to prevent the destruction of such structures, designers usually follow so-called strength reserve approach, which results in a significant increase in the mass of individual parts and, as a consequence, in an undesirable increase in the total weight of the products, their price and operating costs. Hence, a significant reduction in costs is expected, inter alia, through structure optimization with regard to strength and weight.

The mechanical behavior of materials strongly depends on the loading conditions. The influence of a quasi-static strain rate ranging up to 10 s^{-1} on the mechanical behavior of different titanium alloys has been extensively studied [8–13]. A lot of attention has also been paid to the similar studies on a high-strain-rate (dynamic) testing of Ti-based materials [14–20]. However, some important issues such as an influence of the chemical and phase composition, microstructure, as well as the variation of the strain rate within a wide range, and especially, the combined effect of these have not been studied sufficiently so far. Thus, the goal of present work is a systematic study of a strain rate influence on the microstructure evolution and the mechanical behavior of the commonly used two-phase $\alpha + \beta$ titanium alloy Ti-6Al-4V (wt.%) under a loading condition of compression split Hopkinson pressure bar (SHPB). The results are also compared with the data obtained during the quasi-static compression. Moreover, the behavior of commercial pure titanium, considered as single-phase (h.c.p. lattice) material, is studied in similar conditions compared to Ti-6-4 alloy.

2. Materials and Methods

2.1. Materials and Materials Processing

The Ti-6Al-4V-alloy was studied in two different states, the first state was the alloy obtained via a conventional cast and wrought technology [1]. The second state alloy was produced using a cost-efficient blended elemental powder metallurgy (BEPM) approach [18,19] and was designated in this study as Ti64BEPM. The cast and wrought alloy was purchased in a shape of 10-mm diameter rods from Perryman Company (Houston, PA, USA). Two different metallurgical states of the Ti-based alloy were obtained using conventional heat treatments. Annealing of the alloy at 850 °C for 2 h resulted in obtaining a globular microstructure (GL), whereas annealing at 1100 °C for 0.5 h resulted in obtaining a lamellar structure (LM). The alloys with two different microstructural conditions were marked as Ti64GL and Ti64LM, respectively. Ti64BEPM alloy was obtained by blending the titanium hydride TiH_2 powder (particles size <100 μm) and 60Al-40V (wt.%) master alloy in a powder form (particles size <63 μm) and then cold pressing of the blend in a die at 640 MPa followed by sintering at 1250 °C for 4 h under the vacuum of 10^{-3} Pa. The used sintering conditions provide removal of hydrogen from the material to an admissible level (0.002–0.003%) and transformation of the powder compacts into bulk homogeneous alloy. More details on materials fabrication using the adopted BEPM protocol can be found in [21,22]. The sintered Ti64BEPM samples were bars with dimensions of 9 × 9 × 60 mm. In order to assist the results evaluation and understand an influence of phase and chemical composition on mechanical behavior of the main object, the Ti64 alloy, a comparative analysis was performed on the commercial pure titanium (c.p.Ti) Grade 1. The alloy was purchased in the shape of rods with a diameter of 10 mm from Titan Ltd. (Kyiv, Ukraine).

2.2. Quasi-Static and High-Strain-Rate Tests

The quasi-static tensile properties were determined using INSTRON 3376 strength machine following ASTM E8 standard with specimens having gage diameter 4 mm and gage length 25 mm,

whereas the quasi-static compressive tests were carried out with the use of MTS C45 strength machine. For both types of compression tests, quasi-static and dynamic, cylindrical specimens with a diameter and height of 5 mm were used. The Young, shear moduli, and Poisson's ratio of materials were measured with resonance-frequency-damping analysis (RFDA) apparatus (IMCE, Belgium) using impulse excitation technique in accordance with ASTM E1876-15 Standard.

The high-strain-rate compression tests were performed with the use of a split Hopkinson pressure bar (SHPB), also called a Kolsky bar technique [23–25]. The basic parameters of the SHPB system are shown in Figure 1. The length of the input and output bars was 1200 mm, the length of the striker bar was 250 mm, the diameter of all bars was 12 mm. The bars were made of maraging steel (heat-treated MS350 grade: yield strength—2300 MPa; elastic wave speed—4960 m/s). The striker bar was driven by a compressed air system with the barrel length of 1200 mm and the inner diameter of 12.1 mm. The impact striker bar velocities applied during the experiments were in the range from 10 to 25 m/s, which ensures strain rates in the range of 1100 – 3320 s^{-1} for dimensions of the used specimens.

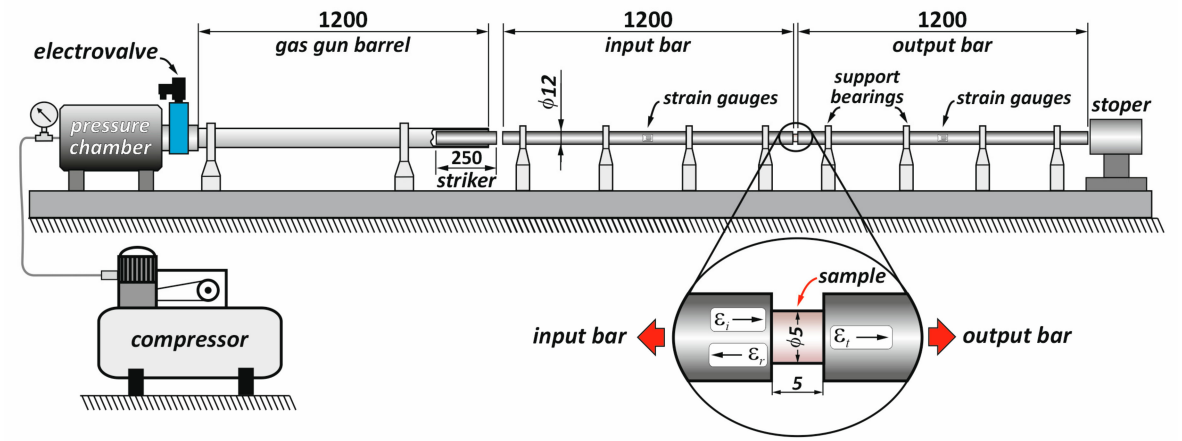

Figure 1. The schematics of the split Hopkinson pressure bar (SHPB) system used in this study.

The plastic flow stress, strain, and a strain rate of the sample were determined according to the classical Kolsky theory [24,25] based on the one-wave analysis method, which assumes stress equilibrium for a specimen under given testing conditions. Wave signals, incident (ε_i), transmitted (ε_t), and reflected (ε_r), were measured by pairs of strain gages (gauge length—1.5 mm; resistance—350 Ohm) glued at the half-length of the input and output bars (Figure 1). The signals from the strain gauges were conditioned with data-acquisition system, composed of Wheatstone bridge, amplifier, and a digital oscilloscope, allowing a high cut-off frequency of 1 MHz.

Strain and a strain rate in the specimens were calculated based on the profile of reflected wave (ε_r) using Equations (1) and (3), respectively, whereas the stress was determined based on transmitted wave (ε_t) (Equation (2))

$$\varepsilon(t) = -\frac{2c_b}{L}\int_0^t \varepsilon_r(t)dt \quad (1)$$

$$\sigma(t) = \frac{A_b E}{A_s}\varepsilon_t\,(t) \quad (2)$$

$$\dot{\varepsilon}(t) = -\frac{2c_b}{L}\varepsilon_r(t) \quad (3)$$

where: L, A_s are the length and the cross-section area of the specimen; E, A_b, c_b are the Young's modulus, the cross-sectional area, and the elastic wave velocity of the pressure bar, respectively.

To minimize dispersion of the wave by damping the Pochhammer-Chree high frequency oscillations and to facilitate the stress equilibrium, a pulse shaping technique was used [26]. The technique consists in placing a small disc made of soft material on the impact end of the

input bar. The disc is often called a pulse shaper or a wave shaper. Plastic deformation of the pulse shaper physically filters out the high frequency components in the incident pulse and modifies its profile. The pulse shaper size needs to be chosen for the given striker impact velocity and mechanical response of tested material. The tests were performed to find the proper size of the pulse shaper in order to obtain stress equilibrium during high-strain-rate deformation of titanium alloy specimens. It was found that for a given SHPB test condition, the copper pulse shaper with a diameter of 3 mm and thicknesses in the range from 0.1 to 0.4 mm (depending on impact striker velocity) guarantees damping of the high frequency oscillations and achieving the dynamic stress equilibrium in the specimen (Figure 2). The typical raw signals recorded during the SHPB experiment are shown in Figure 2a, whereas Figure 2b presents the stresses on the front and back face of the Ti64LM specimen cracked under applied compressive loading. As it can be observed in Figure 2a, the presence of pulse shaper limits significantly a stress fluctuation on incident wave profile. The reflected and transmitted signals are also almost smooth without large oscillations. In turn, the stress-state equilibrium condition presented in Figure 2b is satisfied, i.e., front and back stresses are close throughout the loading history, except a peak at the top of the initial rise and a gap occurring at the end of the loading time. This gap is the result of a crack in the Ti64LM specimen.

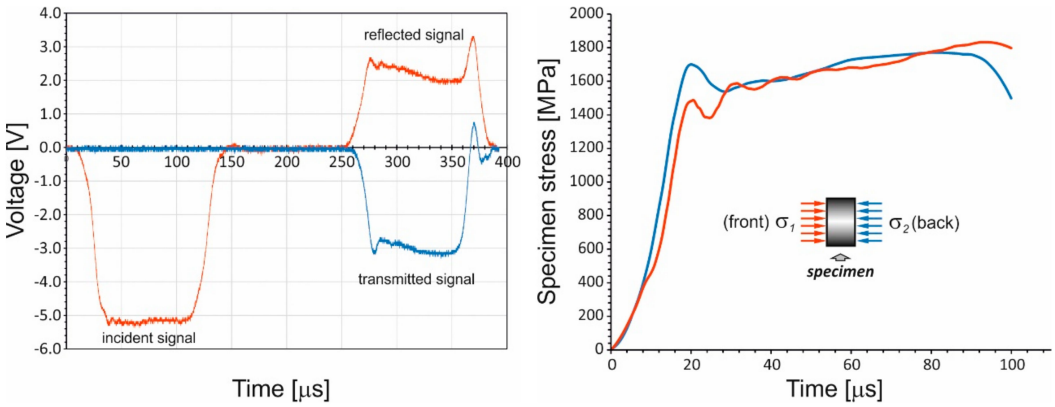

Figure 2. (**a**) Typical raw wave signals from SHPB experiment for Ti64LM; (**b**) stresses on the front and back end of Ti64LM specimen (dynamic stress equilibrium).

Moreover, the grease composed of mineral oil, lithium soap and molybdenum disulfide (MoS_2) was applied to the interfaces between the specimen and the bars to minimize the interfacial friction.

2.3. Microstructural Characterization

The structure of all materials was studied with light optical microscopy (LOM) using XL70 (Olympus, Shinjuku, Tokyo, Japan) and scanning electron microscopy (SEM) using Vega 3 and Mira 3 machines (both from Tescan, Czech Republic). SEM Mira 3 was also used to study the fracture surfaces and electron backscatter diffraction (EBSD) was used to evaluate local crystallographic orientation of different microstructural elements. Metallographic specimens were prepared according to standard grinding and polishing methods [1]. For SEM and EBSD, the final polishing was carried out using Saphir Vibro polisher (ATM, Germany). Some samples were additionally ion polished/etched using PECS model 682 (Gatan, CA, USA) or chemically etched using standard Kroll's solution [1]. The gas content in the sintered specimens was measured using a gas analyzer OH900 (Eltra, Germany).

3. Results and Discussion

3.1. Initial Microstructure Characterization

Typical microstructures of the studied materials are presented in Figure 3, and their chemical compositions are listed in Table 1. Pure titanium c.p.Ti is characterized by relatively coarse α-grain structure with an average size of about 600 μm (Figure 3a). The intragrain substructure is highly developed and is characterized both by the presence of twins and the dislocation network, including formation of cells. Such an extensive structure of defects may result from relatively fast cooling rates used after deformation or annealing (Figure 3a).

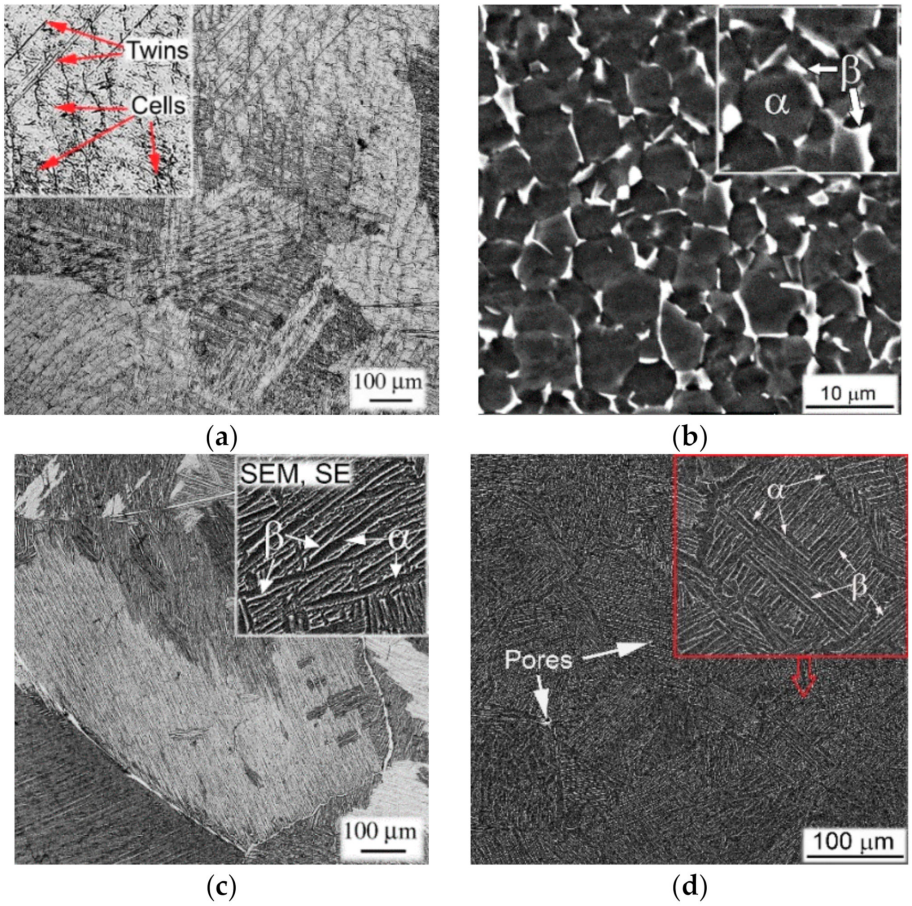

Figure 3. Microstructure of Ti-based materials in the initial state: (**a**) c.p.Ti; (**b**) Ti64GL; (**c**) Ti64LM; (**d**) Ti64BEPM; (**a**,**c**)—LOM; (**b**,**c** (in the corner),**d**)—SEM, SE (secondary electron image).

Table 1. Chemical composition of studied materials.

	Alloying Elements, wt.%					
	Al	**V**	**Fe**	**O**	**N**	**Ti**
c.p.Ti	<0.2	-	<0.08	0.01	0.007	Base
Ti64LM, GL	5.8	3.96	0.21	0.016	0.008	Base
Ti64 BEPM	5.94	4.06	0.16	0.2	0.03	Base

The Ti64GL specimens were of uniform and fine globular microstructure with an average size of α-globules of about 7 μm (Figure 3b), which explains a good balance of the quasi-static tensile strength and ductility (Table 2, #2). The microstructure of the Ti64LM consisted of rather coarse β-grains (average size 800 μm) with coarse (up to 500 μm in some grains) colonies of

α-lamellae inside (Figure 3c), which caused a noticeable decrease in both tensile strength and ductility (Table 2, #3). The Ti64BEPM alloy was also of coarse-grained lamellar microstructure (Figure 3d); however, both β-grains (average size of about 100 μm) and colonies of shorter α-plates were much finer (compare Figure 3c,d), because of a pinning role of residual pores in the grain boundary movement, which prevents from grain coarsening during sintering [18,19]. The Ti64BEPM demonstrates a higher strength compared to the Ti64LM (Table 2, # 4 vs. #3), because of a higher content of impurities (Table 1, #3), and shows lower ductility, which may be also related to the increased impurities content and presence of about 1.5–2 vol.% of residual pores.

Table 2. Mechanical properties of tested materials (tension rate 8×10^{-4} s^{-1}).

##	Tensile Yield Stress [MPa]	Ultimate Tensile Stress [MPa]	El. [1] [-]	RA [2] [-]	Young Module [GPa]	Shear Module [GPa]	Poisson's Ratio	Vickers Hardness [HV]
#1 c.p.-T	345	408	0.38	0.59	111.5	46	0.253	117
#2 Ti64GL	988	993	0.19	0.42	121.7	47	0.275	312
#3 Ti64LM	824	865	0.15	0.31	121.7	47	0.275	309
#4 Ti64BEPM	932	1033	0.08	0.21	123.0	N/A	N/A	339

[1] El.—elongation, [2] RA—reduction in area.

3.2. Mechanical Response

3.2.1. Stress–Strain Behavior

To characterize the base mechanical properties of the tested Ti-based materials, the quasi-static tensile and elastic characteristics are listed in Table 2. The Ti64GL presents the highest yield stress equal to 988 MPa, whereas the Ti64LM presents the lowest one—824 MPa, which is almost 2.4 times higher than the one of c.p.Ti (345 MPa). The Ti64GL material exhibits also the highest ductile properties (elongation 0.19), whereas the Ti64BEPM is characterized by the lowest elongation equal to 0.08. Ductility of all Ti-6-4 alloys tested is relatively low compared to the ductility of c.p.Ti (elongation 0.38).

Stress–strain behavior of the materials tested under uniaxial compression was, as predicted, slightly different. Generally, a compression yield point at a quasi-static strain rate for all materials was at the same or slightly lower level (349, 918, 938, and 879 MPa, for ## 1, 2, 3, and 4 in Table 2, respectively). An exception was the Ti64LM, which demonstrated a higher yield stress in compression than in tension. In turn, fracture of the specimens at the quasi-static compressive regime occurred at significantly higher strain values, i.e., Ti64LM and Ti64BEPM cracked at strain of 0.28 and 0.42, respectively, whereas c.p.Ti and Ti64GL did not fracture before reaching the strain of 0.5, at which the compression was stopped.

Similar dependencies in the specimen damage behavior under compression was observed in dynamic testing conducted at strain rates in the range from 1250 to 3320 s^{-1}. With the exception of c.p.Ti, all other materials cracked under dynamic loading; however, cracking occurred at lower strain values compared to the corresponding quasi-static test results, and it will be discussed in the further part of the paper. In Figure 4a, a few high-speed video frames are presented to illustrate typical successive stages of the specimen deformation process, i.e., the start (Figure 4a-1), the uniform deformation (Figure 4a-2), onset of specimen barreling (Figure 4a-3), intensive local heating, fracturing crack, and the spark flash at the final stage of the deformation (Figure 4a-4). In turn, Figure 4b shows a typical view of the cracked specimens after the quasi-static and dynamic compression.

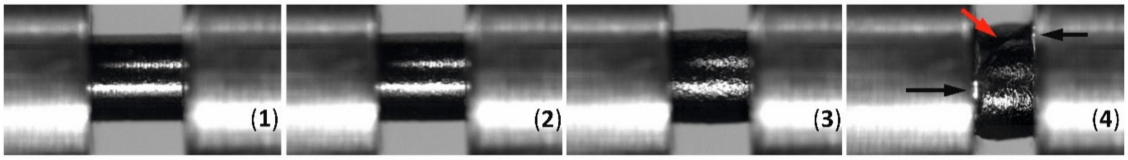

(**a**)

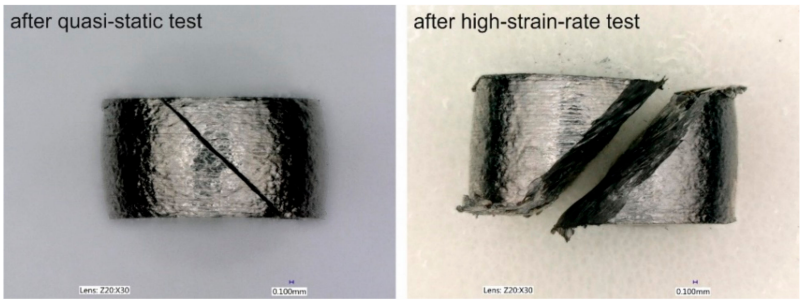

(**b**)

Figure 4. (**a**) High-speed video frames illustrating plastic deformation and fracture of the Ti64BEPM specimen during of the SHPB test at the strain rate of 2100 s^{-1}: the start—(**1**), uniform strain—30 μs (**2**), barreling onset—60 μs (**3**), specimen cracking—120 μs (**4**)—arrows indicate: fracture crack—red arrow, and a areas of intensive local heating on the contact surface with the bar—black arrow; (**b**) view of the cracked specimen of Ti64BEPM after quasi-static and high-strain-rate tests in compression.

The true stress–strain curves of the tested Ti-based materials compressed at quasi-static and high-strain-rates ranges are shown in Figure 5. A number of important observations can be based on these results. First of all, the initial peak stress and oscillations visible on the curve for the highest strain rate are not a real mechanical response of the material, but they result from technical limitations of the SHPB technique. However, the stress–strain curves oscillations were significantly reduced through applying a pulse shaper technique and, in the case of the SHPB experiments with lower strain rates, the obtained stress–strain curves are smooth and almost without oscillation. Second, the quasi-static stress–strain curves reveal differences in the strain hardening behavior of the tested materials (Figure 5e). The strain hardening coefficient n, calculated from a slope of a fitting line of the true stress–strain curve plotted on a logarithmic scale (assumed ranges of plastic strain—0.05–0.2 or 0.05–0.4), is the highest for the Ti64GL (0.148). The values of n for the Ti64LM and Ti64BEPM are relatively lower, and equal to 0.052 and 0.068, respectively. The c.p.Ti demonstrates the highest value of n coefficient, 0.334, as it was expected. Third, the work hardening behavior of the materials tested under high-strain-rate loading is similar to quasi-static loading; however, strain hardening effect is slightly reduced through the heat generation during the dynamic compression, which leads to the flow softening at high strains. This phenomenon seems to be the most pronounced for the Ti64GL and Ti64BEPM. It should be noted here that conversion of the deformation energy to the thermal energy is not uniform throughout the specimen volume, particularly at the end of the sample deformation stage. Careful observation of the high-speed camera films allowed detection of the intense heating and the strain localization near the contact surfaces of the specimen with the front surfaces of the bars (bright areas marked with black arrows in Figure 4a-4). This intense local heating is also manifested by the outflow of a part of the material on the sample side surface (see the image on the right side in Figure 4b).

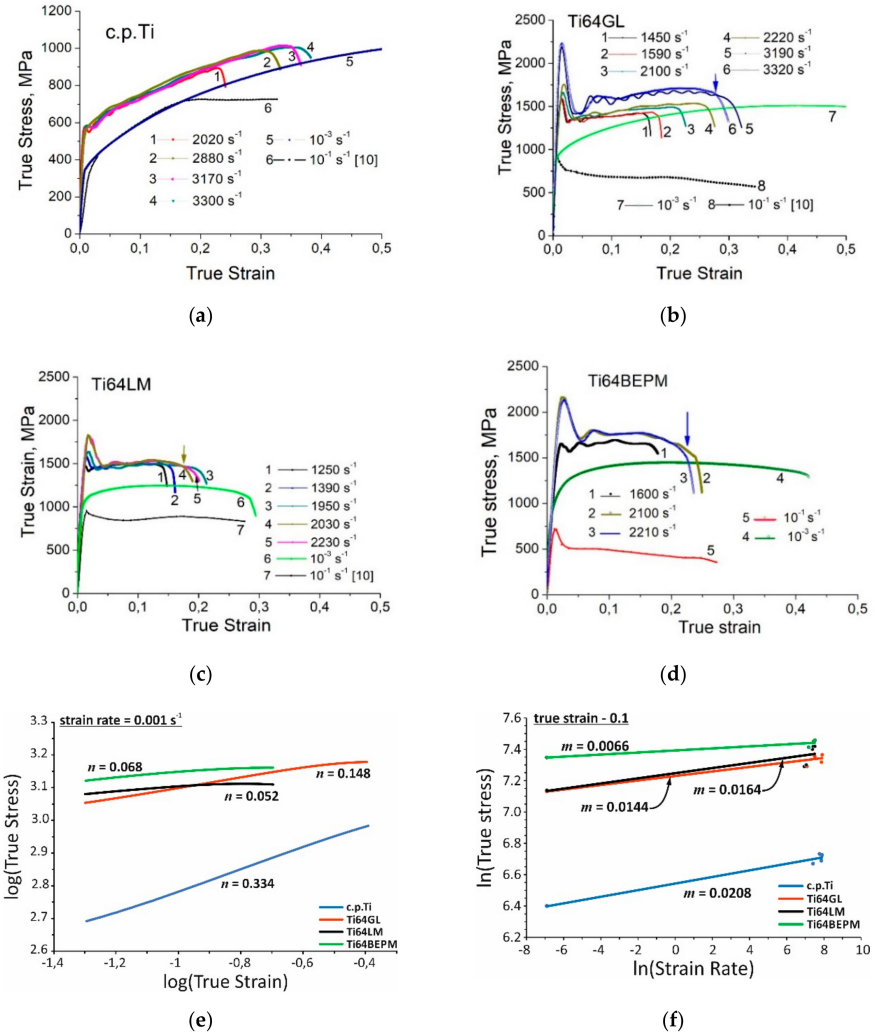

Figure 5. Quasi-static and dynamic stress–strain curves and the calculated mechanical data for: (**a**) c.p.Ti; (**b**) Ti64Gl; (**c**) Ti64LM; (**d**) Ti64BEPM (arrows in (**b**,**d**) indicate possible moment of fracture for relevant curves); (**e**) strain hardening coefficient—n; (**f**) strain rate sensitivity exponent—m.

As it was expected, the plastic flow stress levels at dynamic regime are significantly higher in comparison to the ones at quasi-static regime. The highest peak flow stress (a maximum stress in the plastic range of deformation) is presented by the Ti64BEPM (1770 MPa at strain of 0.17) and the Ti64GL (1700 MPa at strain of 0.23), whereas the Ti64LM reveals the lowest peak flow stress equal to 1540 MPa at 0.12. In the case of c.p.Ti, the peak flow stress, corresponding to unloading of incident wave, is at the level of 1000 MPa at strain of 0.35. In turn, analysis of values of the strain rate sensitivity exponent m (Figure 5f), calculated from the slopes of linear regressions (Equation (4)), shows the highest flow stress increase with an increasing strain rate for the Ti64LM (m = 0.0164). The strain rate sensitivity of Ti64GL is slightly lower (m = 0.0144), whereas the Ti64BEPM demonstrates the lowest one (m = 0.0066). The value of m factor for c.p.Ti is relatively high (0.0208) compared to the other alloys examined.

$$m = \mathrm{d}(\ln(\sigma_t))/\mathrm{d}\left(\ln\left(\dot{\varepsilon}\right)\right) \tag{4}$$

where σ_t is the true flow stress at strain of 0.1, and $\dot{\varepsilon}$ is average strain rates.

As it was noted earlier, cracking the Ti alloys tested under the dynamic loading occurred at lower strain values compared to the corresponding quasi-static test results. However, it was observed (see Table 3) that specimens deformed with the critical strain rates (at which cracking occurred)

damage at lower strains (ε_{cr}) than specimens tested with slightly lower strain rates without cracking (strain designation—ε_{max}). For example, the Ti64GL specimen tested at a strain rate of 3190 s^{-1} achieved a strain value equal to 0.30 (curve #5 in Figure 5b), while an analogous specimen deformed at 3320 s^{-1} cracked at a slightly lower strain equal to 0.28 (curve #6 in Figure 5b). The same dependency was found for Ti64LM and Ti64BEPM.

Table 3. Comparison of ε_{cr} and ε_{max} for the tested Ti-alloys.

	Ti64GL	Ti64LM	Ti64BEPM
strain ε_{cr} at $\dot{\varepsilon}$ (s^{-1})	0.28 (3320)	0.17 (2030)	0.23 (2210)
strain ε_{max} at $\dot{\varepsilon}$ (s^{-1})	0.30 (3190)	0.19 (1950)	0.24 (2100)

Based on the data listed in Table 3, it can be concluded that the Ti64LM alloy exhibits the lowest value of ε_{cr} at the strain rates slightly above 2000 s^{-1} compared to Ti64BEPM and Ti64GL materials, which crack at strains of 0.23 and 0.28 and at strain rates of 2210 and 3320 s^{-1}, respectively. It should be emphasized that resistance to cracking of the Ti64GL alloy under the dynamic deformation is significantly higher compared to other Ti-alloys tested.

3.2.2. Material Strain Energy

In order to carry out more in-depth assessment of the mechanical behavior of the materials tested under dynamic loading, an additional parameter, i.e., strain energy (*SE*), was used. It is a convenient parameter that allows comparing the mechanical response of materials tested with various methods and strain rates [11–13]. The *SE* is defined as the internal work performed to deform a material specimen through an action of the externally applied forces. The *SE* was determined by integrating the area under the stress–strain curve (for integration limits from zero to ε_{upper}). In the case of the cracked specimens, a value of ε_{upper} corresponded to a value of strain at fracture, whereas for the non-cracked specimens, ε_{upper} was assumed to be equal to strain at the moment of the specimen unloading (sharp drop in stress–strain curve). The upper integration limit ε_{upper} for the non-cracked specimens under quasi-static loading was assumed to be 0.5.

As it can be seen in Figure 6a, the cast and the wrought alloy Ti64 in both the globular and the lamellar microstructural states have almost the same values of *SE* at the strain rates up to 2000 s^{-1} (curves 2 and 3 in Figure 6a). However, above this strain rate level, the Ti64LM cracked in contrast to the Ti64GL, which demonstrated the highest level of *SE* among all materials studied.

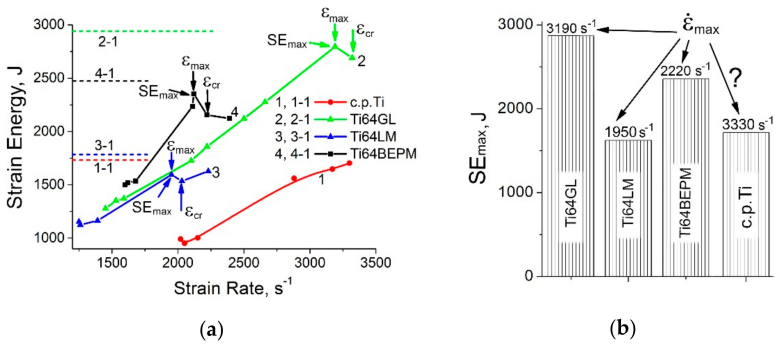

Figure 6. The strain energy for the studied Ti-based materials: (**a**) *SE*-strain rate dependence; (**b**) comparison of the maximum strain energy values (SE_{max}) corresponding to the maximal strain rate $\dot{\varepsilon}_{max}$ (indicated by arrows), for which specimens do not crack during the SHPB tests.

A change from cast and wrought to BEPM in the method for manufacturing the Ti64 alloy significantly affected the measured *SE* values. The Ti64BEPM material revealed a higher ability to store mechanical energy at strain rates up to 2300 s^{-1}. The *SE* values were noticeably higher

compared to Ti64GL, and at the strain rate range of 2100–2300 s^{-1}, at which Ti64BEPM specimens broke (compare curves 4, 2 and 3; Figure 6a).

It is also interesting to compare the *SE* values calculated from the quasi-static and the high-strain-rate tests data. The maximal *SE* value determined at quasi-static tests (horizontal (1-1) line in Figure 6a) is approximately equal to the SE_{max} level obtained for the maximum strain rate ($\dot{\varepsilon}_{max}$) for c.p.Ti only (curve #1 in Figure 6a). In turn, *SE* values for Ti64 alloys in all microstructural states from the quasi-static tests (horizontal lines (2-1), (3-1), and (4-1) in Figure 6a) are slightly higher than the SE_{max} values obtained for the whole range of strain rates, at which specimen cracking occurred (marked by arrows on curves 2–4 in Figure 6a).

Since the main difference between the studied Ti64 structures was the β- grain size, the SE_{max} values (Figure 6b) were related to the grain size of the tested Ti-alloy. From the data presented in Table 4 it can be seen that a larger β-grain size in Ti64 alloy structure causes a decrease in SE_{max}.

Table 4. Dependency between SE_{max} parameter and β-grain size of the tested Ti64 alloys.

	Ti64GL	Ti64LM	Ti64BEPM
grain size [μm]	7	800	160
strain energy SE_{max} [J]	2795	1594	2354

It is also worth noting that c.p.Ti has—as predicted—the lowest *SE* value among all studied materials and at all strain rates. The *SE* value for c.p.Ti is almost twice lower compared to the cast and wrought alloys, despite the pure titanium shows very high plasticity, because of which specimen fracture does not occur at the applied strain and strain rates (curve 1 in Figure 6a).

In view of the fact that titanium alloys are often used instead of other structural materials in various critical applications, the results of the present study were additionally compared to similar data of other commonly used structural materials [27] (Figure 7). The lowest level of the *SE* parameter (Figure 7a) demonstrates the aluminum alloy B95 (curve 1), as it was expected. The high-strength steels ARMOX 600T and Docol 1500M are characterized by significantly higher *SE* values (curves 2, and 3), which exceed the corresponding values for Ti64GL and Ti64BEPM alloys at the same strain rates (curves 5, and 6). However, when these curves were converted considering the density of tested materials (Al alloy B95—2850 kg/m^3 [28], for all Ti-based materials—4500 kg/m^3 [1], and for steels of 7850 kg/m^3 [29]), results revealed another dependency between considered materials (Figure 7b).

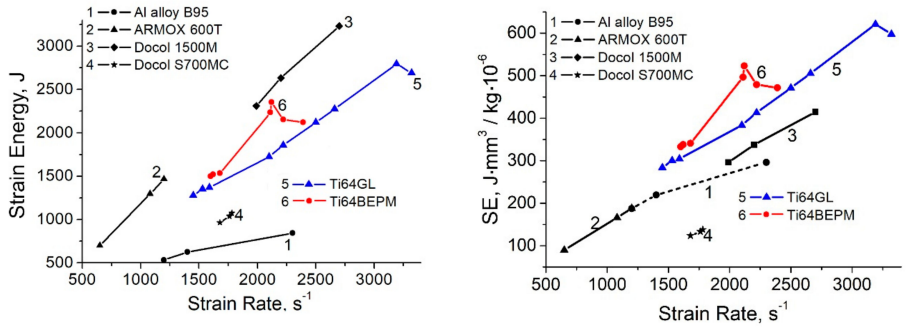

(**a**) (**b**)

Figure 7. Comparison of the SE-strain rate dependencies for different materials: (**a**) absolute values of the SE; (**b**) relative (specific) values of the SE. The data used for the curves 1–4 were taken from [27].

It can be clearly seen that the aluminum alloy at the strain rates of about 1500 s^{-1} is not worse than ARMOX 600T steel (curves 1, and 2), whereas titanium-based materials are undeniably better than the high-strength steels (curves 5–7). The only, rather serious, drawback of the BEPM made titanium materials is that they could be cracked at relatively low strain rates. However, such a shortcoming could

be overcome, at least partially, by incorporating these materials into multilayer structures combining them with high ductility Ti64 alloy layers in the optimized configuration, as it was shown in a few studies published earlier [30,31].

3.3. Deformed Microstructures Investigation

Analysis of the microstructure of materials formed during plastic deformation is a primary step to evaluate a difference in their mechanical behavior. The initial examination of the structural features of all the specimens after quasi-static tests and high-strain-rate SHPB deformation allows identification of four main zones distinguished by the stress state and, as a result, having specific differences in the microstructure (Figure 8). Zone I is quite narrow and is characterized by tangential shear stresses caused by the interaction on the contact surfaces of the specimen and SHPB bars. Zone II tracks across the entire specimen at an angle of approximately 45° to the vertical axis of the cylinder and it corresponds to the plane of the maximum shear stresses in accordance with Schmid law [32]. This zone is characterized not only by the maximum shear stresses, but also by the greatest strain localization, due to stress collapse, adiabatic shear band (ASB) initiation, temperature rise and crack formation [11,16,19]. Zone III is adjacent to zone II and it corresponds to the secondary strain localization, where ASBs and secondary (smaller) cracks were also observed. Zone IV is located away from the fields of intense stresses and strain localization; however, the stress state in this zone is more complicated, involving the compressive stress along the vertical axis of the cylinder sample and tensile (or shear) perpendicular to it.

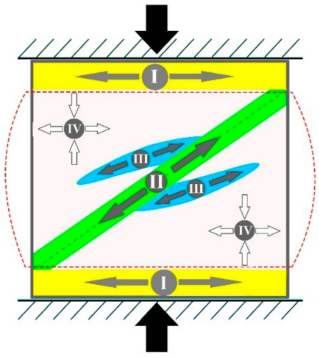

Figure 8. Schematic representation of specific zones distinguished in the longitudinal section of tested cylindrical specimen (Roman number denote a given zone; the arrows indicate the direction of compressive force).

3.3.1. Microstructure Analysis of c.p.Ti

The microstructure of c.p.Ti after SHPB tests is shown in Figure 9a,b. The numerous plastic deformation traces, in the form of slip bands, twins, and well-developed substructure inside α-phase plates, are observed in all zones near the specimen-to-bar contact surfaces (Figure 9a) as well as across the entire bulk of the specimen (Figure 9b). A comparison with the initial not-deformed state (Figure 3a) shows a significant increase in defects density, while a general character of the substructure remains approximately the same. Assuming that titanium with single-phase h.c.p. lattice could easily deform by twinning at sufficiently low temperatures [1,33,34], it was expected that defected areas should contain mainly twins. However, given the probability of a significant local increase in temperature during the deformation [18,35], a few other scenarios should not be excluded, namely, the formation of a well-developed dislocation substructure and the possibility of the phase transformations, including the martensite formation, as it was reported in [36,37], where c.p.Ti was subjected to fast heating and cooling. Eventually, because of the high plasticity of c.p.Ti, introduction of some deformation defects could not be completely excluded for this alloy as a result of sample preparation (after delicate ion polishing and/or etching), although their presence causes a "background" effect in all the samples

made of this alloy. Nevertheless, the areas of localized deformation and ASB were not found in c.p.Ti specimens, even in those tested at the highest strain rates (Figure 9b).

The microstructure after the quasi-static tests seems to be uniform in all zones. It is modified by plastic deformation, showing a higher density of deformation defects and a smaller size of cells and twins (Figure 9c,d). This results from different strain rates used at quasi-static tests (0.001 s^{-1}) and SHPB tests (3200 s^{-1}); difference is more than 6 orders. Therefore, under the quasi-static tests, there are more possibilities and longer time for material relaxation compared to SHPB experiments.

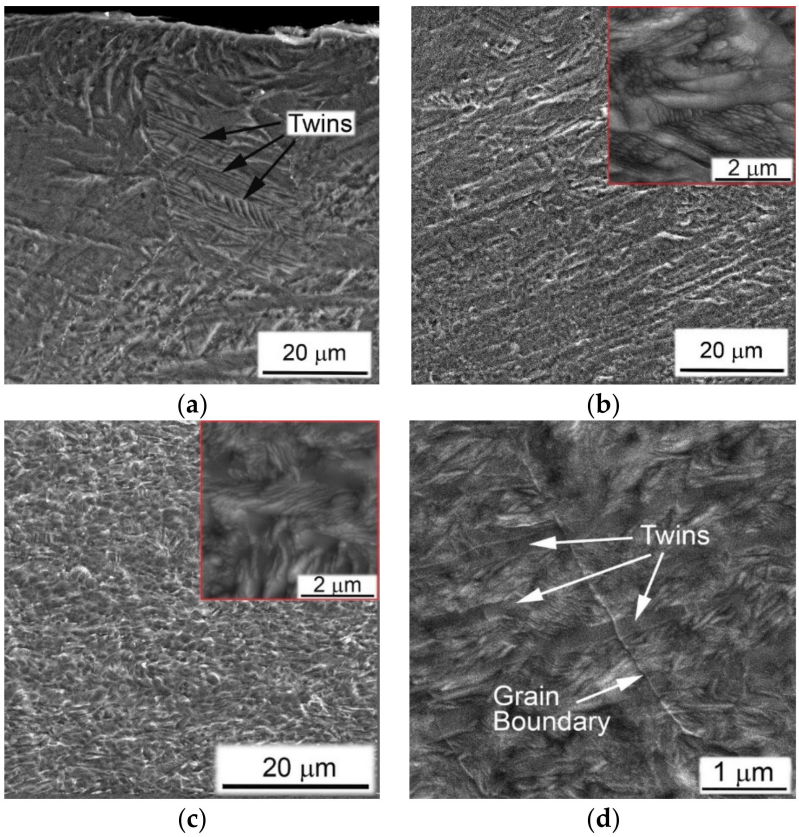

Figure 9. SEM images of c.p.Ti specimens sectioned along the longitudinal direction of the cylinders after: (**a**,**b**) SHPB test at the strain rate of 3200 s^{-1}—(**a**) near the zone I, (**b**) in the center of zone II; (**c**,**d**); quasi-static test with the strain rate 0.001 s^{-1}—zone 4. SEM, SE.

3.3.2. Microstructure Analysis of Ti64GL

Typical images of Ti64GL microstructure after SHPB tests, which did not cause fracture of specimens, can be seen in Figure 10. In general, the microstructure of this material did not change significantly in bulk after compression at 2100 s^{-1}, without failure, compared to the initial state. In some local micro-volumes, a couple of twins in the separate globules were observed closer to the specimen core (zones II and IV, Figure 10b). More significant traces of plastic deformation were observed in thin (5–7 μm) surface layers in zones I (Figure 10a), which could be a consequence of localized deformation, due to interaction between the surfaces of the specimens and the bars. An increase in a compression rate up to 2500 s^{-1} (Figure 10c) or even to 2660 s^{-1} (Figure 10d–f) also did not cause failure of the specimens, but led to a noticeable change in their microstructure. In this case, more than a half of all α-globules (about 65%) contain deformational twins, and they are observed in all zones throughout the bulk of the specimen. According to [1,33,34], during compression, the {11–22} twins are first formed inside the grains with the c-axis oriented parallel to the loading direction, and afterwards the formation of the {10–11} twins occurs in the grains oriented differently. Therefore, it appears that with an increase in compression strain rates, new twinning planes are activated inside the α-globules. Delicate etching

of the deformed specimens reveals, in addition to twins, fine dislocation cells (their size is not more than a few tens of nanometers) observed in both α- and β- phases (Figure 10e,f).

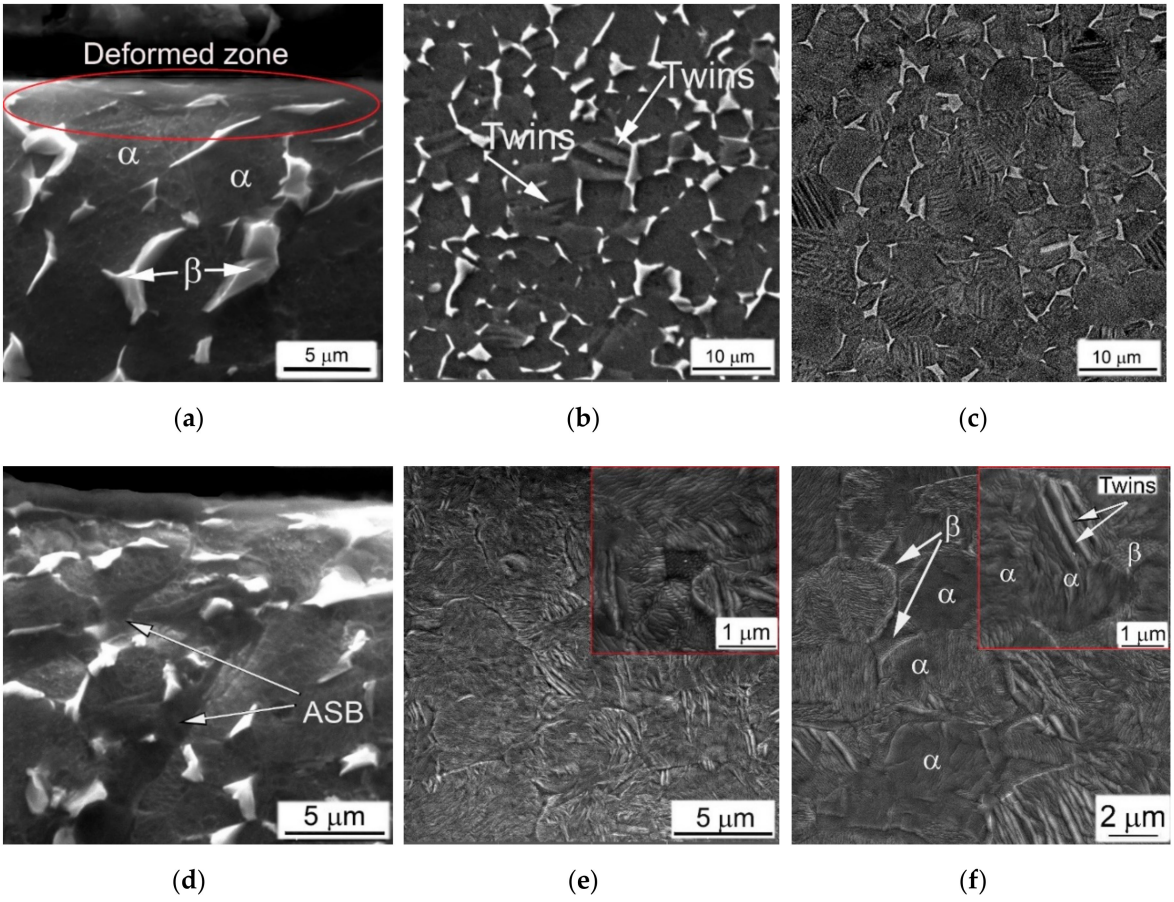

Figure 10. SEM images of Ti64GL specimens after the dynamic tests at the following strain rates: (**a**,**b**) 2100 s^{-1}; (**c**) 2500 s^{-1}; (**d**–**f**) 2660 s^{-1}—(**a**,**d**) show zone I; (**b**,**c**)—zone IV; (**e**,**f**)—zone III; (images (**a**,**b**,**d**–**f**) are taken in SE mode from the etched surface, whereas image (**c**) is in the BSE (back scattered electrons) mode from just polished surface.

A further increase in a strain rate up to 3320 s^{-1} caused cracking of the Ti64GL specimen, and appearance on the fracture surface (Figure 11a) small melted areas (Figure 11b) and dimples (Figure 11c), which are characteristic for ductile fracture. It should be emphasized that the main crack propagated in the unchanged direction (Figure 11a), which is clearly noticeable by the configuration of ductile grooves on the entire fracture surface (Figure 11c). There is also noticeable secondary or lateral crack propagation (indicated by B in Figure 11a) on both sides of the main crack fracture (indicated by A) and forms distinct relief.

The internal microstructure of the samples is distinct from the above-discussed cases of testing with low strain rates. There are multiple primary ASBs observed in zone II, on the edges along the entire main crack (Figure 11d,e). Finer secondary ASBs spreading out of the main crack at a certain direction were also found in zone III (Figure 11f). A much fewer number of twins are observed in zone III (Figure 11d,g) compared to the cases of deformation with low strain rates. Moreover, a lot of structural elements of completely different morphology were revealed. The extremely fine (not larger than 0.1 μm × 2.2 μm) needle-shaped elements are formed within individual globules, as it is shown in the top right corner of Figure 11d. Such crystals could be a result of crystallographically ordered transformation, as it was reported in [34]. Their shape and orientation suggest martensitic needles, considering that the individual needles are located at an angle of approximately 60° relative to each

other. It is probable that in proximity of zones of the localized extreme heat, where the temperature can reach the single-phase region (about 1000 °C) [18,19], and primary α- phase was transformed into high-temperature β-phase. In such a case, the transformation takes place without redistribution of alloying elements between neighboring initial crystallites of α- and β- phases, because of extremely high heating and cooling rates. A similar mechanism of the structure formation takes place during laser heating [38,39] and, because of subsequent fast cooling, this metastable β-phase can transform into low-temperature α′-martensite.

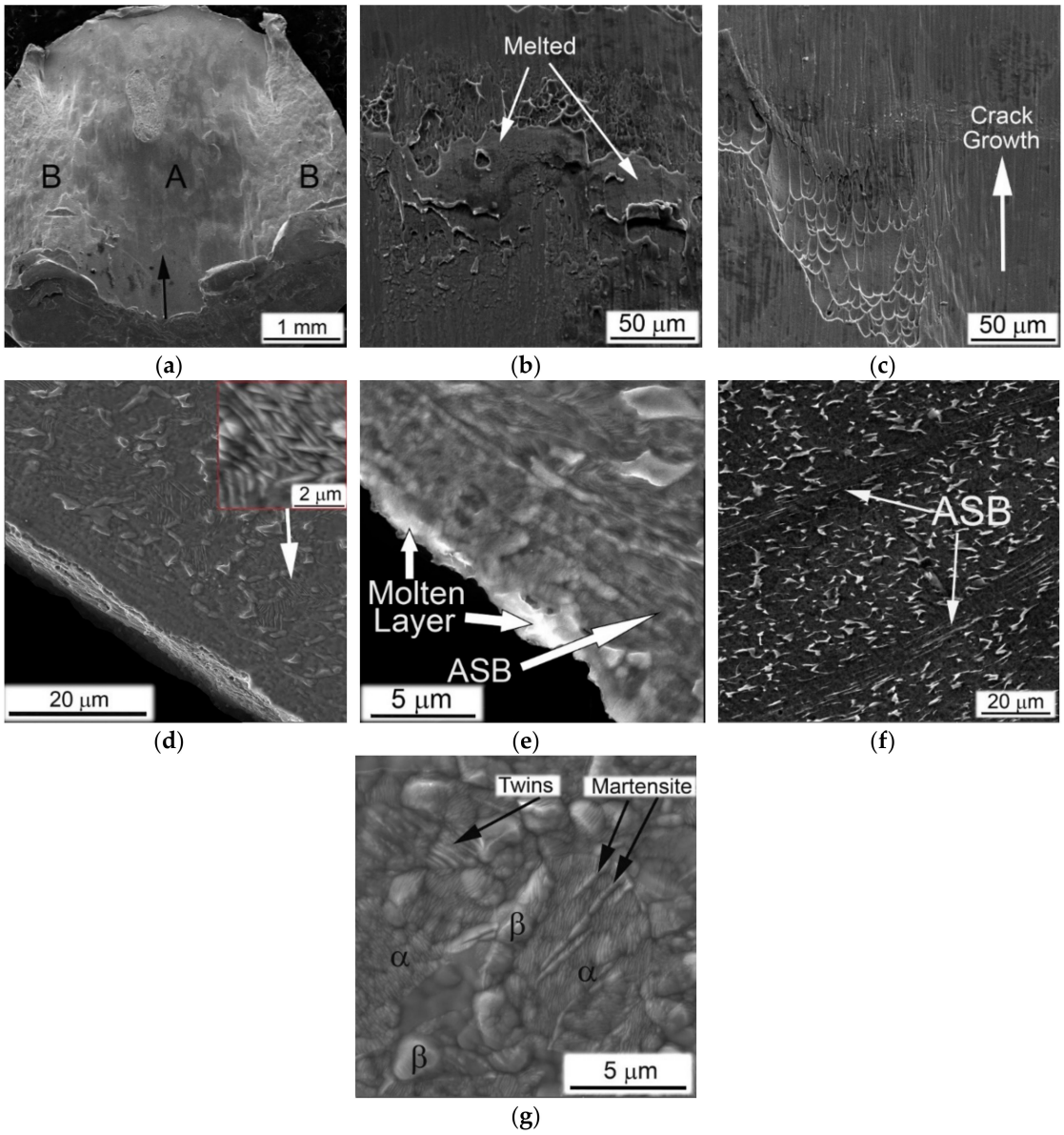

Figure 11. SEM images of the fracture surface (**a**–**c**), and the internal microstructure (**d**–**g**) of the Ti64GL specimen tested under the strain rate of 3330 s^{-1}; A—main crack spread, B—secondary cracking; (**d**) and (**e**)—zone II; (**f**)—zone III with secondary ASBs coming from the main crack; (**g**)—zone IV. The arrow in (**a**) indicates the direction of the crack propagation from its nucleation site. SEM, SE.

Bearing in mind a small size of tested specimens and their contact with massive input and output bars, the cooling process should be relatively rapid. It is probable that a pure (neat shear without any contribution of diffusion) martensitic transformation under these thermo-mechanical conditions does not take place, and a transformation of bainite type could easily take place, when diffusion of alloying

elements could have happened during phase transformation, but most importantly Ti atoms move in an ordered way. A similar case was described for the Ti-6Al-4V alloy before experiments when the cooling rate from single β-phase temperatures was changed gradually; however, complete suppression of diffusion was established upon cooling at 400 °C per second [40]. When the cooling rates are lower, the shear transformation occurred with the involvement of diffusion and redistribution of alloying elements. This fact may explain a slightly unusual morphology of the observed martensite crystals (Figure 11d,g).

Microstructure of Ti64GL after the quasi-static tests presents distinct differences compared to the SHPB tests structure. The existed phase constituents, α-phase globules and β-phase interlayers, are flattened perpendicularly to the loading direction through almost the entire specimen volume (Figure 12). All the tested specimens did not crack, and thin bands of localized slip/shear were found in zone II of maximum localized strain (Figure 12a). The microstructure shows the same character of the flattened phase constituents in all other locations (zones III and IV); however, the images of high magnification reveal greater plastic deformation in α-phase compared to β interlayers (Figure 12b).

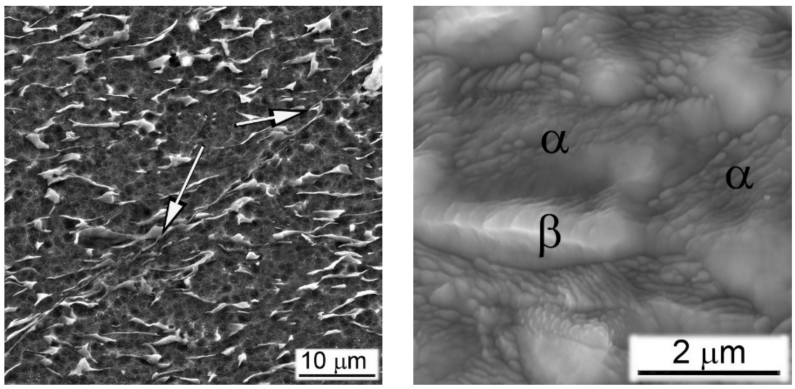

(**a**) (**b**)

Figure 12. Microstructure of the non-cracked Ti64GL specimen after the quasi-static test at the strain rate of 0.001 s^{-1}: (**a**)—zone II, (**b**) zone IV. SEM, SE. Arrows in (**a**) indicate a slip localization band.

3.3.3. Microstructure Analysis of Ti64LM

The Ti64LM specimens deformed at strain rates for which fracture occurred show distinct plastic deformation in zone I on one side of the specimen (Figure 13a) as well as cracks on the other side (Figure 13b). It is probable that these cracks are initiated at β-grain boundaries reaching the specimen fracture surface and decorated [12] by α-phase layer. It should be noted that outside Zone I there is no significant evidence of plastic deformation in α-plates and their packets; however, small cracks were found within Zones II and IV (Figure 13c,d, respectively). These cracks are not associated with any structural elements such as β-grains boundaries, α-phase colonies, or α/β interlayers. These cracks easily crosscut the α-phase plates, partially deflecting on the α/β interlayers (Figure 13c), and finally move outside the individual plates (Figure 13d). The observed crack propagation insensitivity to structural elements appears to be remarkable since the microstructure of titanium alloys usually plays a pivotal role in the crack nucleation and growth under conditions of the quasi-static tension [1,11–13,41].

The fracture of the Ti64LM specimens under the SHPB test condition was observed at a strain rate of 2030 s^{-1}. A typical image of the crack surface and the microstructure in its vicinity are shown in Figure 14. The surface of the crack shows a typical ductile fracture disclosing multiple tear-off/shear dimples (Figure 14a). However, the zone adjacent to the crack surface on the section cut perpendicular to the crack shows rather unique features (Figure 14b). There are no evidences of plastic deformation at all, even close to the edge of the crack. Except slightly melted edge of the sample in the zone II, the structure in bulk of the sample is unchanged compared to initial condition (compare Figures 14b and 3c). This observation suggests that plastic deformation of the Ti64LM alloy becomes highly

localized with an increase in the strain rate. The Ti64LM specimen deformation reaches its critical values slightly above 2000 s^{-1}, when the fracture occurs.

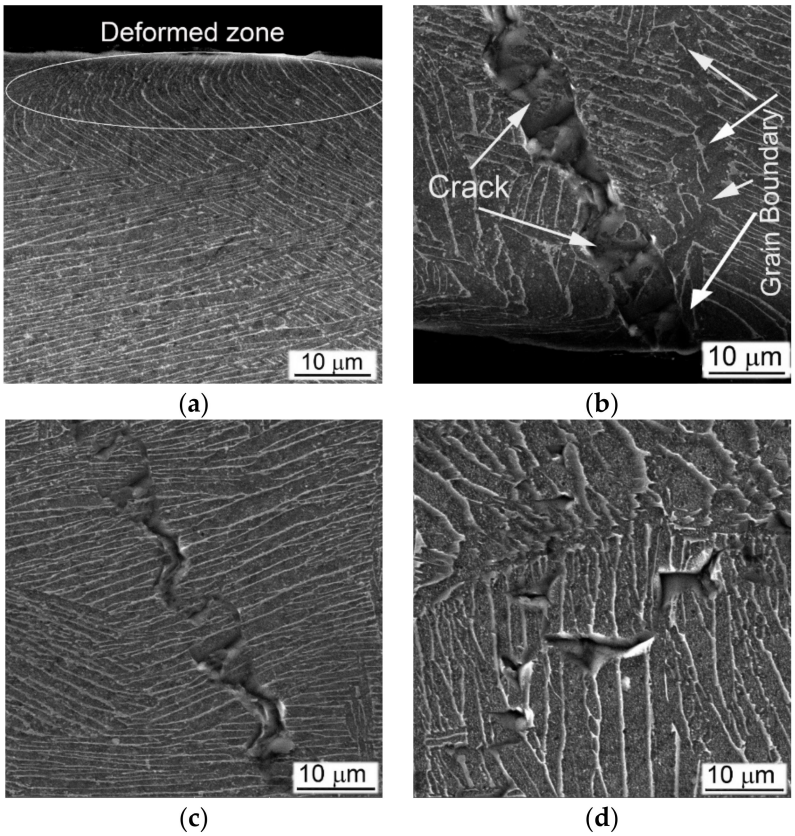

Figure 13. Microstructure of the Ti64LM specimen after SHPB test at the strain rate of 1390 s^{-1}: (**a**,**b**)—zone I, (**c**)—zone II, (**d**)—zone IV. SEM, SE.

The following conclusions can be drawn from comparison analysis of the Ti64GL and the Ti64LM structures subjected to the dynamic loading conditions. The principal difference between these two structural states is defined by configuration and extent of a/β interphase boundaries. The Ti64GL, similarly to c.p.Ti, has predominantly α/α boundaries that appear to facilitate a relatively free propagation of plastic deformation (flow) through the material even at high strain rates despite the fact that majority of neighboring globules present essentially different crystallographic orientation [1]. On the contrary, the Ti64LM boundaries between microstructural elements are almost on 100% presented by interphase α/β boundaries that remarkably prevent a free spread of deformation due to hindering of dislocation movement. It results in an increased strain localization and concentration of the stress, which may enable a cavity nucleation and, conclusively, fracture at an increased strain rate.

The SEM-EBSD analysis of Ti64LM specimen after the SHPB test with a strain rate of 2030 s^{-1} is presented in Figure 15. Kikuchi patterns, required to obtain EBSD data, were distinctive in many points near the contact (fracture) surface. However, Kikuchi lines were not identified by the software, which may result from significant distortions caused by high residual stresses remained in the material after the dynamic plastic deformation. Since the annealing, required to relieve these stresses, would inevitably lead to significant changes in the fine structure of the material resulting in polygonization or recrystallization, it was not carried out. The orientation map shows substantially non-uniform plastic deformation of the structure resulting from the test and clearly reveals few zones where deformation is localized. The β-phase cannot be resolved because of its size and morphology. It is represented by thin layers (from few tens to hundreds of nm) in between relatively thicker (a few m) α-lamellae and considering their likely tilt toward the analyzed surface the β-phase resolution becomes

an unsolvable challenge for EBSD even the one operating with field-emission gun SEM, which was the case [42]. A significant number of the noise pixels, mostly aligned along the α-lamellae, result from unsuccessful orientation measurement of the β-phase. Because of the same reason, the individual α-lamellae also cannot be distinguished on the orientation map; however, it is clearly seen in the band contrast image, nonetheless the packers are easier to be traced on the orientation map plot. Some of the packets demonstrate significant misorientation of lamellae within the packet. For instance, a pink and purple packet, 40-m thick, on the left edge of the image shows approximately 10 deg. bent within a few m span. A big yellow and pink packet at the bottom of the image shows even bigger misorientation suggesting big dislocation density accumulated within some small zones. This image also demonstrates short secondary cracks originating outside of the main crack (Figure 15a), which indicate that crack nucleation is not related to such important microstructural elements as grain or interphase boundaries, and crack can nucleate inside a single α-lamella (see the left crack in Figure 15b).

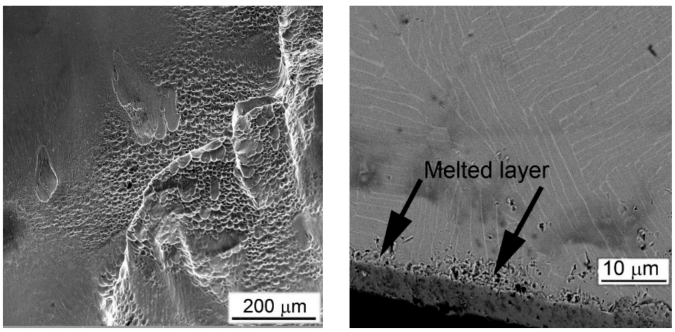

(**a**) (**b**)

Figure 14. Microstructure of the cracked Ti64LM specimen after SHPB tested at the strain rate of 2030 s^{-1}: (**a**) fracture surface (SEM, SE); (**b**) microstructure in zone II (polished, not etched) (SEM, BSE).

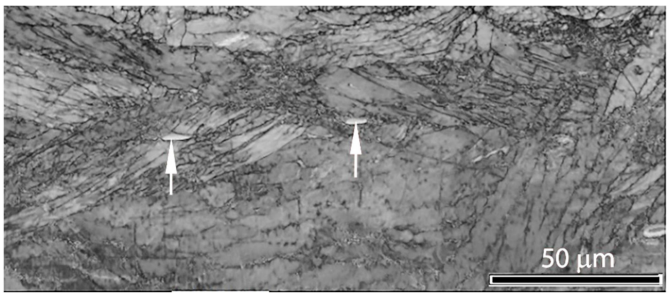

(**a**)

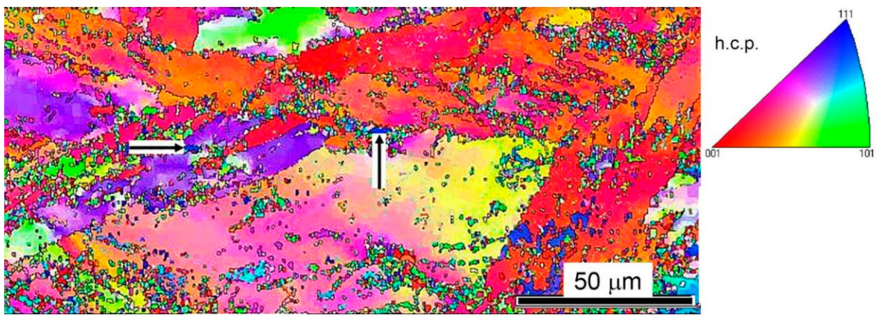

(**b**)

Figure 15. The SEM-EBSD images of Ti64LM specimen SHPB tested at 2030 s^{-1}: (**a**) band contrast image, (**b**) EBSD orientation map - arrows indicate small secondary cracks appeared inside α-lamellas.

The decisive impact of the compressive strain rate on plastic deformation localization is underlined by the results of the quasi-static tests of Ti64LM specimens (Figure 16). The plastic strain localization becomes more visible during compression at the strain rate of 0.001 s^{-1}. It resulted in the appearance of a considerably narrow zones crossing the sample at an angle of 45°, where maximum strain was localized, and finally causing the main crack nucleation which, in turn, initiated the secondary cracks (Figure 16a). These secondary cracks often cut and shift the individual grains. The α-layer, labeled with A in Figure 16b, wrapping the initial β-grain, was sheared by the crack in the direction perpendicular to this α-layer. The microstructure after the test (Figure 16c) is not much different compared to the initial structure (Figure 3c), except a few cracks seen in zones IV; however, a detailed examination reveals a complex substructure of multiple twins and dislocation slip traces inside the α-phase plates (Figure 16d).

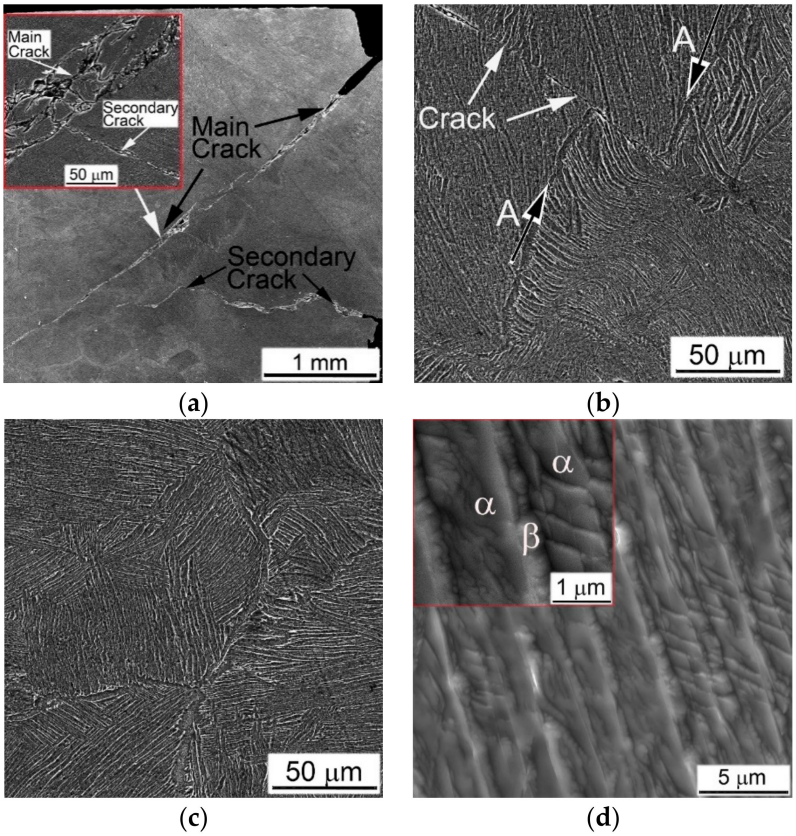

Figure 16. Microstructure of the Ti64LM specimen after the quasi-static test at the strain rate of 0.001 s^{-1}: (**a**) general view with zones I and II, (**b**)—zone III, (**c**,**d**)—zone IV. SEM, SE.

The processes of plastic deformation on micro- (inside separate α- and β-phases crystallites) and macro-level (at least a group of crystallites involved in cooperative response) should be distinguished which means that the dissipation of the total strain energy can be prioritized differently depending on the real structure. The alloy Ti64LM under slow quasi-static compression technically deforms in the same way as in the case of dynamic impact loading. Under such a condition, a smaller strain energy portion is apprehended at the micro-level in a form of plastic deformation localized inside α-lamellas, while its major fraction dissipates at the macro-level and is localized within a small zone. On the contrary, in the Ti64GL alloy, the strain energy is more apprehended at the micro-level, and no distinction between micro- and macro-level of energy dissipation is observed in c.p.Ti.

3.3.4. Microstructure Analysis of Ti64BEPM

Similarly to the cast and wrought Ti64LM, the Ti64BEPM alloy deformed at high strain rates demonstrates plastic deformation mainly in zone I, primarily on the samples that did not crack (Figure 17a). Moreover, the intense plastic deformation also took place locally, for example, in grain boundaries, and it was recognized as shear deformation (Figure 17b). Furthermore, the deformed (collapsed) residual pores were observed in various locations (Figure 17a). The diagonal zone II across the specimens was not found.

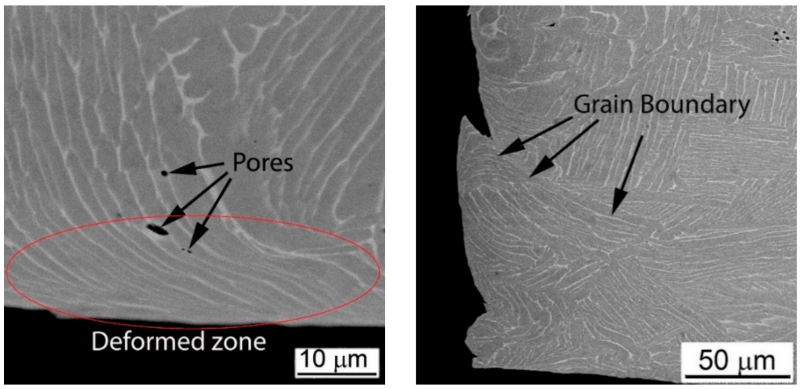

(**a**) (**b**)

Figure 17. Microstructure of the non-cracked Ti64BEPM specimen tested at the strain rate of 2100 s^{-1}: (**a**) plastic deformation in zone I; (**b**) shear deformation in the vicinity zone I. SEM, BSE.

The microstructure of the Ti64BEPM alloy, after the test, was almost the same as the one of the Ti64LM discussed before. In zone I, similarly to the previous cases of the Ti64LM and Ti64BEPM (not fractured specimen—Figure 17), a plastically deformed layer of approximately the same depth (up to 20–30 m) was observed (Figure 18c). The main crack propagates in zone II through the entire specimen at an angle of 45° toward its vertical axis. Zone II itself is thin, not more than 5–6 m, and the ASB are formed on the sample fracture edges (Figure 18d). A number of pores collapsed and multiple α-lamellae and β-interlayers are curved due to the plastic flow of the material in vicinity of the crack (Figure 18d). Small secondary cracks initiated on the β-grain boundaries and α-colony boundaries are observed in zone III (Figure 18e). There is no evident plastic deformation in zone IV, except some slightly deformed pores partially flattened perpendicular to the direction of the applied load (Figure 18f). However, more detailed images of the slightly etched ion-beam samples reveal a fine needles microstructure inside the α-plates (Figure 18g,h). The formation of such an inner plate substructure is unique, and the observation of the uniform triangle arrangement of the needles with a uniform 60° angle between them (Figure 18h) is typical for martensite in h.c.p. lattice metals [37]. As it was mentioned before, a similar microstructure was also observed in the Ti64GL specimen fractured at the strain rate of 3330 s^{-1} (Figure 11d). Such a structure may result from rapid heating of the material during the impact, when the α-phase plates transformed into the high-temperature β-phase in such a fast way that the redistribution of alloying elements between the initial α- and β-phases did not occur. It is confirmed by the clear interphase boundary between the β-phase and the α-phase lamellar region, which includes the needles (Figure 18g). The area outlined by the circle in Figure 18h is of particular interest since it shows the intersection of the needles lying in the plane of the polished surface and perpendicular to it.

A general view of the fracture surface of the cracked Ti64BEPM specimen compressed at the strain rate of 2220 s^{-1} (Figure 18a) is similar to the fractures of the Ti-6-4 alloy with both globular (Figure 11a) and lamellar microstructure (Figure 14a). The fracture also demonstrates a rectilinear zone of the main crack growth (A in Figure 18a) and two side zones of the secondary crack propagation (B, ibid.). The images of higher magnification show the residual pores (Figure 18b), and their presence

in the structure makes Ti64BEPM alloy essentially different from the cast and wrought Ti64LM alloy (Figure 14a).

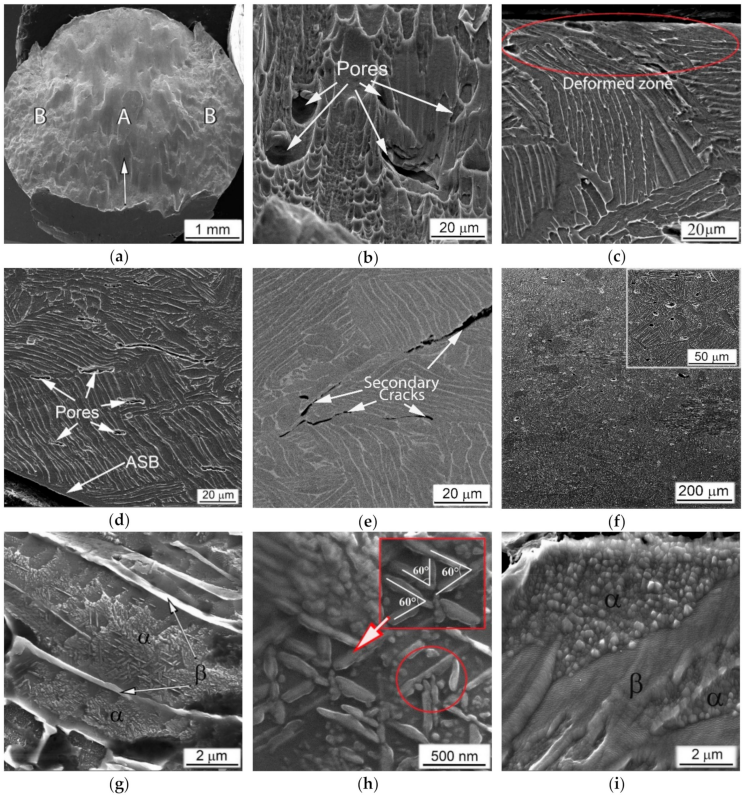

Figure 18. The SEM images of the fracture surface of the Ti64BEPM specimen tested at the strain rate of 2220 s^{-1}: (**a**); general view; (**b**) residual pores at fracture surface; (**c**–**i**) internal microstructure; (**c**) zone I, (**d**) zone II; (**e**,**f**) zone III; (**g**–**i**) zone IV; (the arrow in (**a**): indicates direction of the crack growth from nucleation site; (A) and (B) label the fields of main and secondary cracks propagation, respectively). (**a**–**e**,**g**–**i**) SE; (**f**) BSE.

It should be noted that the needles, due to the ion etching, do not demonstrate perfectly smooth boundaries as they should for the martensite structure. The formation of a martensite structure during plastic deformation at the strain rate of up to 2000 s^{-1} was also reported on titanium Ti-8.5Cr-1.5Sn alloy [35], although in that case the observed structure was deformation-induced high-alloyed α"-martensite that formed simultaneously with the twins. The present study case is also different from the case of a fast laser heating [35], because formation of martensitic needles appeared inside of the α-plates with their apparently unchanged outlines (Figure 18g). The observed result can be explained by the fact that, in addition to rapidly changing temperature, a complex stress state also acted on particular zones within the specimen. Such a complex and combined effect is probably responsible for the formation of the martensite in localized volumes and, as a result, at least three variants of Burgers orientation relationships from 12 allowed are clearly seen. It should be emphasized that martensite-like needle crystals were not frequently well revealed. They do not appear to be distinct and they are similar to those shown in Figure 18i. However, it is implicit that the clear view of the martensite needles depends on the "successful" coincidence of planes of their location with the prepared specimen's section that is not highly probable.

The microstructures of the Ti64BEPM alloy after the quasi-static test were characterized by the main crack appeared in zone II surrounded by the secondary cracks appeared on different microstructural elements (Figure 19a). The other deformation features uniformly distributed throughout the specimen were the collapsed residual pores and strongly bent α-lamellae (Figure 19b). Moreover, a cellular dislocation substructure was observed inside the curved lamellae of the α- phases (Figure 19c), similar to

that observed in the case of the Ti64LM specimen after the identical quasi-static test (Figure 16b). This was expected since there is no significant heating taking place in material deformed at a low strain rate, and there is also enough time for more complete stress relaxation in the areas outside of the zone II.

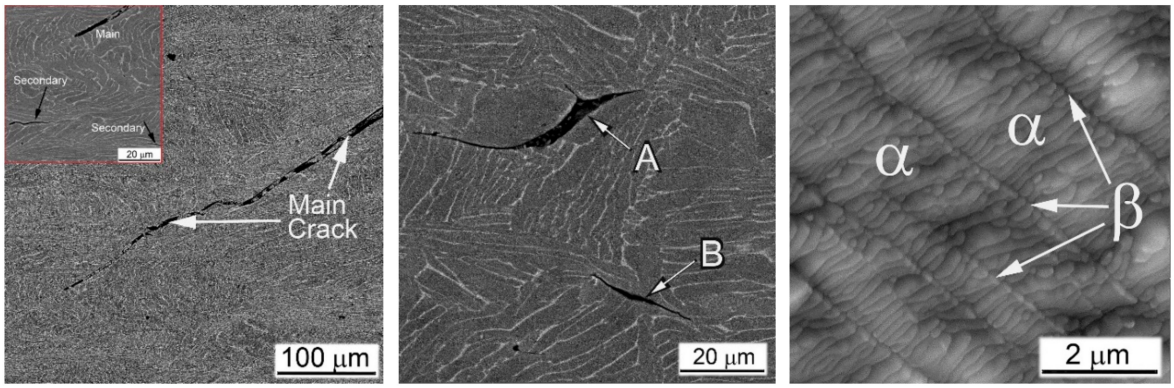

Figure 19. The SEM images of the fractured Ti64BEPM specimen after the quasi-static tests at the strain rate of 0.001 s^{-1}: (**a**) main crack—zone II; (**b**) collapsed residual pores—zone II; (**c**) cellular dislocation substructure inside the curved lamellae of the α-phases—zone IV. (**a**,**b**) BSE, (**c**) SE.

As it was shown in Section 3.1, there is a significant difference in the mechanical behavior of the Ti64LM and Ti64BEPM alloys. Based on the microstructural analysis presented above, different mechanical behavior of the tested Ti-based materials could be explained as follows. Both alloys present a similar type of microstructure, which is represented by relatively coarse β-grains with the colonies of lamellar α-phase inside. However, in detail, they are considerably different with a number of features, such as different sizes of both β- grains (more than 500 m in the Ti64LM vs. 100 m in the Ti64BEPM) and intragrain α-lamellae, the presence of residual pores in the Ti64BEPM, as well as the content of impurities (see Table 1). The high oxygen content as well as high nitrogen content in the Ti64BEPM led to an increase in strength, compared to the Ti64LM, and combined with residual pores of the Ti64BEPM significantly reduces its ductility under the tensile loading (Table 2). However, under quasi-static and dynamic compression the porous Ti64BEPM alloy shows noticeably better characteristics compared to the Ti64LM (Figure 5d,c). It could be explained by the fact that, under the tension loading, the pores work as the stress concentrators and/or crack initiation sites, particularly, when the pore shape is not globular, and the matrix alloy lacks the ductility. However, the pores impact on a deformation mechanism and the material damage process under compression is slightly different. The pores become flattened or even completely collapsed and, thence, play the role of additional "soft" phase without generating stress concentration zones, therefore general compressive plasticity of the porous material is determined by the plasticity of the matrix. Moreover, according to studies [43–45], a positive effect of porosity on the structure sustainability under compression can be amplified by their higher content; the most effective deformation energy absorption was reported at a porosity value of around 60% [46,47].

4. Conclusions

Based on presented experimental data and their analysis the following conclusions are drawn:

(a) Compressive mechanical behavior of titanium alloys is strongly dependent on the phase composition and microstructure of both the studied materials and the applied strain rate level.

(b) The mechanical behavior of a two-phase α + β Ti-6-4 alloy strongly depends on the type and coarseness of the microstructure. The fine-grained Ti-6-4 alloy with a globular (equiaxed) microstructure is more ductile and has the high reserve of plasticity, which allows it to deform

without fracture at the strain rate below 3320 s^{-1}. The critical compression strain rate, at which the fracture occurred, falls to 2030 s^{-1}, when the microstructure changed from globular to coarse-grained lamellar. The observed significantly different mechanical behavior of two structures can be explained by the nature of the interface boundaries between the structural constituents involved in plastic deformation transmission, i.e., the α/α interphase boundaries are prevalent in the globular microstructure, while α/β boundaries are predominant in the lamellar microstructure.

(c) The Ti-6-4 alloy fabricated using BEPM demonstrates the reduced the size of β-grains and intragrain α- lamellae compared to the alloy with a coarse-grained lamellar microstructure produced using a conventional cast and wrought approach. The Ti64BEPM alloy demonstrates a considerably better balance of strength and plasticity under the quasi-static and dynamic compression tests, because of its finer microstructure despite of the presence of about 2% (vol.) of residual pores and higher content of impurities (oxygen and nitrogen). The residual pores do not play any negative role under compression loading in contrary to tension, since they do not work as stress concentrators.

(d) Strain energy was used as a parameter to compare mechanical behavior of the studied materials. It was established that the two-phase Ti-6-4 alloy with a globular microstructure demonstrates the highest value of SE_{max}, which implies the largest reserve of deformability of this alloy under the compression impact at the strain rates. The Ti64 alloy produced using BEPM demonstrates a lower value of the SE_{max} parameter. The Ti64 alloy with coarse lamellar microstructure reveals the lowest values SE_{max}.

(e) It was found that the strain rates increase up to 2200 s^{-1} cause a change in the strain localization mechanism in Ti64BEPM alloy from the macro-level (plastic flow in the sample volume, formation of adiabatic shear bands and cracks) to the micro-level (deformation within individual α-phase lamellae).

(f) The structures of all the studied materials demonstrate more uniform plastic deformation and the absence of its micro-level strain localization after quasi-static compression compared to the dynamic loaded structures.

(g) The Ti-6-4 alloys with a globular microstructure, fabricated using ingot metallurgy, and the Ti64BEPM alloy demonstrate higher relative (specific) *SE* values than B95 aluminum alloy, ARMOX 600T armor steel, or AHSS steel Docol 1500M.

Author Contributions: Conceptualization, validation and project administration, P.E.M., J.J.; methodology, P.E.M., J.J., D.G.S., M.A.S.; formal analysis, V.I.B., S.V.P.; experiments and investigation, P.E.M., J.J., O.O.S., V.I.B., K.C., P.D., M.A.S.; writing—original draft preparation, P.E.M.; writing—review and editing, J.J., D.G.S., V.I.B., S.V.P.; visualization, O.O.S.; All authors have read and agreed to the published version of the manuscript.

Funding: This research received no special funding. Present studies were performed according the Agreement of Cooperation between G.V. Kurdyumov Institute for Metal Physics of N.A.S. of Ukraine and Jarosław Dąbrowski Military University of Technology, Poland. Some separate works were financed by N.A.S. of Ukraine within the frames of the research project #III-09-18. S.V.P. acknowledges funding from the NATO Agency Science for Peace and Security (#G5030).

Conflicts of Interest: The authors declare no conflict of interest.

References

1. Luetjering, G.; Williams, J.C. *Titanium*, 2nd ed.; Springer: Berlin/Heidelberg, Germany, 2007.
2. Williams, J.C.; Boyer, R.R. Opportunities and Issues in the Application of Titanium Alloys for Aerospace Components. *Metals* **2020**, *10*, 705. [CrossRef]
3. Niinomi, M. Recent metallic materials for biomedical applications. *Met. Mater. Trans. A* **2002**, *33*, 477–486. [CrossRef]
4. Fanning, J. Military Application for b Titanium Alloys. *J. Mater. Eng. Perform.* **2005**, *14*, 686–690. [CrossRef]
5. Montgomery, J.S.; Wells, M.G.H.; Roopchand, B.; Ogilvy, J.W. Low-cost titanium armors for combat vehicles. *JOM* **1997**, *49*, 45–47. [CrossRef]

6. Fanning, J. Ballistic Evaluation of Titanium Alloys Against Handgun Ammunition. In *Ti-2007, Science and Technology, Proceedings of the 11th World Conference on Titanium, Kyoto, Japan, 3–7 June 2007*; The Japan Institute of Metals Publish.: Tokyo, Japan, 2007; Volume 1, pp. 487–490.
7. Gooch, W. Potential Applications of Titanium Alloys in Armor Systems. In *Titanium-2011*; International Titanium Association: San Diego, CA, USA, 2011; Available online: https://www.researchgate.net/publication/292328353_Potential_Applications_of_Titanium_Alloys_in_Armor_Systems_-2011 (accessed on 20 October 2020).
8. Stefansson, N.; Weiss, I.; Hutt, A.J. *Titanium'95: Science and Technology*; Blenkinsop, P.A., Evans, W.J., Flower, H.M., Eds.; The University Press: Cambridge, UK, 1996; Volume 2, pp. 980–987.
9. Bhattacharjee, A.; Ghosal, P.; Gogia, A.; Bhargava, S.; Kamat, S. Room temperature plastic flow behaviour of Ti–6.8Mo–4.5Fe–1.5Al and Ti–10V–4.5Fe–1.5Al: Effect of grain size and strain rate. *Mater. Sci. Eng. A* **2007**, *452*, 219–227. [CrossRef]
10. Markovsky, P.; Matviychuk, Y.; Bondarchuk, V. Influence of grain size and crystallographic texture on mechanical behavior of TIMETAL-LCB in metastable β-condition. *Mater. Sci. Eng. A* **2013**, *559*, 782–789. [CrossRef]
11. Markovsky, P.; Bondarchuk, V.; Herasymchuk, O. Influence of grain size, aging conditions and tension rate on the mechanical behavior of titanium low-cost metastable beta-alloy in thermally hardened condition. *Mater. Sci. Eng. A* **2015**, *645*, 150–162. [CrossRef]
12. Markovsky, P.; Bondarchuk, V.I. Influence of Strain Rate, Microstructure and Chemical and Phase Composition on Mechanical Behavior of Different Titanium Alloys. *J. Mater. Eng. Perform.* **2017**, *26*, 3431–3449. [CrossRef]
13. Markovsky, P.E. Mechanical Behavior of Titanium Alloys under Different Conditions of Loading. *Mater. Sci. Forum* **2018**, *941*, 839–844. [CrossRef]
14. Peirs, J.; Verleysen, P.; Degrieck, J.; Coghe, F. The use of hat-shaped specimens to study the high strain rate shear behaviour of Ti–6Al–4V. *Int. J. Impact Eng.* **2010**, *37*, 703–714. [CrossRef]
15. Zheng, C.; Wang, F.; Cheng, X.; Liu, J.; Fu, K.; Liu, T.; Zhu, Z.; Yang, K.; Peng, M.; Jin, D. Failure mechanisms in ballistic performance of Ti–6Al–4V targets having equiaxed and lamellar microstructures. *Int. J. Impact Eng.* **2015**, *85*, 161–169. [CrossRef]
16. Morrow, B.; Lebensohn, R.; Trujillo, C.; Martinez, D.T.; Addessio, F.; Bronkhorst, C.A.; Lookman, T.; Cerreta, E. Characterization and modeling of mechanical behavior of single crystal titanium deformed by split-Hopkinson pressure bar. *Int. J. Plast.* **2016**, *82*, 225–240. [CrossRef]
17. Yin, W.; Xu, F.; Ertorer, O.; Pan, Z.; Zhang, X.; Kecskes, L.; Lavernia, E.J.; Wei, Q. Mechanical behavior of microstructure engineered multi-length-scale titanium over a wide range of strain rates. *Acta Mater.* **2013**, *61*, 3781–3798. [CrossRef]
18. Zhou, T.; Wu, J.; Che, J.; Wang, Y.; Wang, X. Dynamic shear characteristics of titanium alloy Ti-6Al-4V at large strain rates by the split Hopkinson pressure bar test. *Int. J. Impact Eng.* **2017**, *109*, 167–177. [CrossRef]
19. Guo, Y.; Ruan, Q.; Zhu, S.; Wei, Q.; Lu, J.; Hu, B.; Wu, X.; Li, Y. Dynamic failure of titanium: Temperature rise and adiabatic shear band formation. *J. Mech. Phys. Solids* **2020**, *135*, 103811. [CrossRef]
20. Sreenivasan, P.R.; Ray, S.K. Mechanical Testing at High Strain Rates. In *Encyclopedia of Materials: Science and Technology*, 2nd ed.; Elsevier: New York, NY, USA, 2001; pp. 5269–5271.
21. Ivasishin, O.M.; Anokhin, V.M.; Demidik, A.N.; Savvakin, D.G. Cost-Effective Blended Elemental Powder Metallurgy of Titanium Alloys for Transportation Application. *Key Eng. Mater.* **2000**, *188*, 55–62. [CrossRef]
22. Ivasishin, O.; Moxson, V. Low-cost titanium hydride powder metallurgy. *Titan. Powder Metall.* **2015**, *8*, 117–148. [CrossRef]
23. Chen, W.; Song, B. *Split Hopkinson (Kolsky) Bar: Design, Testing and Applications*; Springer: Berlin/Heidelberg, Germany, 2011.
24. Kolsky, H. Propagation of Stress Waves in Linear Viscoelastic Solids. *J. Acoust. Soc. Am.* **1965**, *37*, 1206. [CrossRef]
25. Kolsky, H. Stress waves in solids. *J. Sound Vib.* **1964**, *1*, 88–110. [CrossRef]
26. Panowicz, R.; Janiszewski, J.; Kochanowski, K. The non-axisymmetric pulse shaper position influence on SHPB experiment data. *J. Theor. App. Mech.* **2018**, *56*, 873–886. [CrossRef]
27. Janiszewski, J. *Unpublished Experimental Data Report*; Jarosław Dąbrowski Military University of Technology: Warsaw, Poland, 2020.

28. Database of Steel and Alloy (Marochnik). Available online: http://www.splav-kharkov.com/en/e_mat_start.php?name_id=1448 (accessed on 21 September 2020).
29. Nilsson, M. *Constitutive Model for Armox 500T and Armox 600T at Low and Medium Strain Rates*; Technical Report FOI-R-1068-SE; Swedish Defence Research Agency: Stockholm, Sweden, 2003; Available online: https://www.foi.se/rest-api/report/FOI-R--1068--SE (accessed on 21 September 2020).
30. Markovsky, P.E.; Savvakin, D.G.; Ivasishin, O.M.; Bondarchuk, V.I.; Prikhodko, S.V. Mechanical Behavior of Titanium-Based Layered Structures Fabricated Using Blended Elemental Powder Metallurgy. *J. Mater. Eng. Perform.* **2019**, *28*, 5772–5792. [CrossRef]
31. Prikhodko, S.V.; Ivasishin, O.M.; Markovsky, P.E.; Savvakin, D.G.; Stasiuk, O.O. Chapter 13: Titanium Armor with Gradient Structure: Advanced Technology for Fabrication. In *Advanced Technologies for Security Applications*; Springer: Dodrecht, The Netherlands, 2020; pp. 127–140.
32. Schmid, E.; Boas, W. *Plasticity of Crystals, Special Reference to Metals*; Springer US: New York, NY, USA, 1968.
33. Partridge, P.G. The crystallography and deformation modes of hexagonal close-packed metals. *Metall. Rev.* **1967**, *12*, 169–194. [CrossRef]
34. Ma, C.; Wang, H.; Hama, T.; Guo, X.; Mao, X.; Wang, J.; Wu, P. Twinning and detwinning behaviors of commercially pure titanium sheets. *Int. J. Plast.* **2019**, *121*, 261–279. [CrossRef]
35. Yang, H.; Wang, D.; Zhu, X.; Fan, Q. Dynamic compression-induced twins and martensite and their combined effects on the adiabatic shear behavior in a Ti-8.5Cr-1.5Sn alloy. *Mater. Sci. Eng. A* **2019**, *759*, 203–209. [CrossRef]
36. Markovsky, P.; Semiatin, S. Microstructure and mechanical properties of commercial-purity titanium after rapid (induction) heat treatment. *J. Mater. Process. Technol.* **2010**, *210*, 518–528. [CrossRef]
37. Banerjee, S.; Mukhopadhyay, P. Phase Transformations: Examples from Titanium and Zirconium Alloys. *Pergamon Mater. Series* **2007**, *12*, 1–813.
38. Markovsky, P.E. Two-stage transformation in (α+β) titanium alloys on non-equilibrium heating. *Scr. Met. Mat.* **1991**, *25*, 2705–2710. [CrossRef]
39. Semiatin, S.L.; Obstalecki, M.; Payton, E.J.; Pilchak, A.L.; Shade, P.A.; Levkulich, N.C.; Shank, J.M.; Pagan, D.C.; Zhang, F.; Tiley, J.S. Dissolution of the Alpha Phase in Ti-6Al-4V During Isothermal and Continuous Heat Treatment. *Met. Mater. Trans. A* **2019**, *50*, 2356–2370. [CrossRef]
40. Gridnev, V.N.; Ivasishin, O.M.; Markovsky, P.E.; Svechnikov, V.L. The role of the cooling rate in the formation of the structure of titanium alloys thermally hardened with incomplete homogenization of the β phase. *Metallofiz (Phys. Met.)* **1985**, *7*, 37–44. (In Russian)
41. Lütjering, G. Influence of processing on microstructure and mechanical properties of (α+β) titanium alloys. *Mater. Sci. Eng. A* **1998**, *243*, 32–45. [CrossRef]
42. Isabell, T.C.; Dravid, V.P. Resolution and sensitivity of electron backscattered diffraction in a cold field emission gun SEM. *Ultramicroscopy* **1997**, *67*, 59–68. [CrossRef]
43. Kumar, P.; Chandran, K.S.R.; Cao, F.; Koopman, M.; Fang, Z.Z. The Nature of Tensile Ductility as Controlled by Extreme-Sized Pores in Powder Metallurgy Ti-6Al-4V Alloy. *Met. Mater. Trans. A* **2016**, *47*, 2150–2161. [CrossRef]
44. Biswas, N.; Ding, J. Numerical study of the deformation and fracture behavior of porous Ti6Al4V alloy under static and dynamic loading. *Int. J. Impact Eng.* **2015**, *82*, 89–102. [CrossRef]
45. Banhart, J. Manufacture, characterization and application of cellular metals and metal foams. *Prog. Mater. Sci.* **2001**, *46*, 559–632. [CrossRef]
46. Suzuki, A.; Kosugi, N.; Takata, N.; Kobashi, M. Microstructure and compressive properties of porous hybrid materials consisting of ductile Al/Ti and brittle Al3Ti phases fabricated by reaction sintering with space holder. *Mater. Sci. Eng. A* **2020**, *776*, 139000. [CrossRef]
47. Garcia-Avila, M.; Portanova, M.; Rabiei, A. Ballistic performance of composite metal foams. *Compos. Struct.* **2015**, *125*, 202–211. [CrossRef]